IEEE Photonics Journal
An IEEE Photonics Society Publication

Open Access

Perception Oriented Haze Image Definition Restoration by Basing on Physical Optics Model

Volume 10, Number 3, June 2018

Hui Fu
Bin Wu
Yanhua Shao
Hongying Zhang

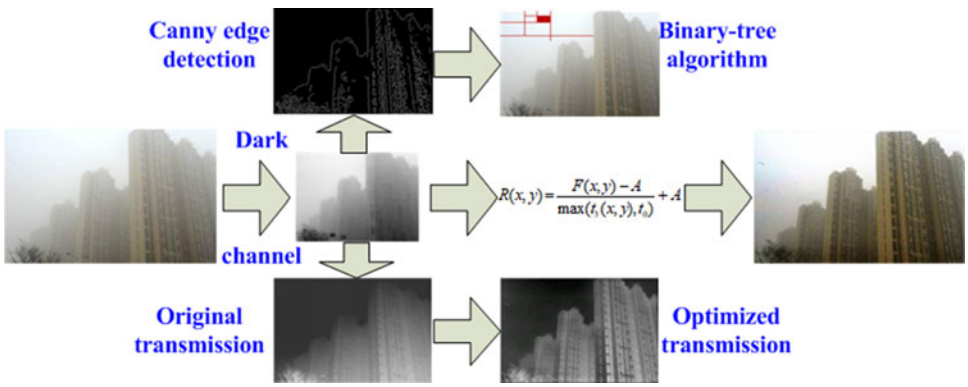

DOI: 10.1109/JPHOT.2018.2837010
1943-0655 © 2018 IEEE

IEEE photonics SOCIETY

IEEE

Perception Oriented Haze Image Definition Restoration by Basing on Physical Optics Model

Hui Fu, Bin Wu, Yanhua Shao, and Hongying Zhang

School of Information Engineering, Southwest University of Science and Technology, Mianyang 621000, China

DOI:10.1109/JPHOT.2018.2837010

Manuscript received March 20, 2018; revised May 8, 2018; accepted May 11, 2018. Date of publication May 18, 2018; date of current version June 8, 2018. This work is supported by the National Natural Science Foundation of China under Grant 61601382, the Scientific Research Fund of SiChuan Provincial Education Department No. 17ZB0454, the Fund of Robot Technology Used for Special Environment Key Laboratory of Sichuan Province under Grant 15kftk05, funded by Longshan academic talent research supporting program of SWUST (17LZX682). Corresponding author: Hui Fu (e-mail: 1285110730@qq.com).

Abstract: Existing haze removal approaches have unreliable estimation of atmospheric light and transmission, which lead to imprecision color information recovery, gradient reversal artifacts, and halo effect. In this paper, a novel haze removal technique based on ambient light model is presented. Our technique applies canny edge detection algorithm which can locate the sky area accurately, and adopts binary-tree algorithm to obtain the radiance of atmospheric light A rapidly; then, an adaptive wiener filter is employed for modifying transmission map, and halo effect is further restricted in the sudden changed region of scene depth by the morphology method. Experimental results verify that the optimized approach has better robustness, and is superior to present methods.

Index Terms: Scattering, imaging, visualization, binary-tree, wiener filter.

1. Introduction

The occurrence of haze strongly degrades the image and vision quality. Besides, dehazing is a real challenge problem owing to its ill conditioning nature. Hence, it is essential to research de-hazing technologies. Over the past years, miscellaneous single image de-hazing techniques have been proposed to promote the visual impact of the contaminated image. Former de-hazing techniques are depended upon extra information not limited to the input image only. These methods perform efficaciously when there contains precise additional information. In effect, however, it can be extremely hard, expensive, or even difficult to acquire such additional information.

Recently, image de-hazing has made significant progress in some particular aspects [1]–[4]. Based on Narasimhan's [2] method, Xie *et al.* [5] built a one dimensional model on the basis of color decay prior, and developed the scene depth assessment formula. The method in Zhong *et al.* [6] adopted Artificial Neural Networks (ANNS) on his image data-set, involves some artificial images, while Li's approach works inferior in dense fog areas. Yet Xie's modality is inclined to be unstable, so the scattering index is not suitable for all images. Rizzi [7] combined white balance technology and supervised machine learning method together to derive transmission. Besides, Rizzi's method brought about a novel idea for single image removal algorithms, while the haze removal result is

circumscribed by unsufficient pattern. What's more, the methods based on physical optics model exist ordinary weakness: the ensemble contrast is low peculiarly for non-uniform illumination images. Finlayson [8] applied a grey tone algorithm which is built upon the norm and low-level features in Minkowski's technology [9], the common weakness of above-mentioned algorithms is that it is can't eliminate the incorrectness of defined arguments.

Although as an ill-posed puzzle, single image haze removing has various kinds of prior techniques. Based on Fattal's work [10], Singh [11] integrated independent component analysis (ICA) with Markov random field (MRF) algorithms to recover the transmission. The effect of this method based on the enough color information, and may fail in monochrome images. Tan [12] presumed clear images have higher contrast than haze images. Based on the postulation, the haze removal algorithm [12] maximize the input haze image contrast extent directly. Nevertheless, this approach may cause hallo effect or excessive enhancement. He [13] put forwarded the famous hypothesis of dark channel prior (DCP), and estimated transmission depending on the observation that the intensity of haze-free pixels normally included at least one RGB color channel being zero or nearly zero. The DCP technique can get impressive dehazing results, while it can't properly process the areas whose luminance is basically similar to the dynamic atmospheric light. In recent years, multifarious DCP-based algorithms [4], [14]–[16] have been developed. Whereas the transmission handled by DCP model is unsmooth and exists image noise. He [17] adopted soft matting algorithm to restrict the block and the halo effect. However, soft matting algorithm consumes a large amount of time, He [18] further used a quite compelling edge-preserving algorithm named guided filter to optimize the transmission, thereby reducing the cost of computation. Tarel [19] assumed atmospheric light value is close to the maximal value in the feasible field, so he estimated the global atmospheric light with median filter and applied an adaptive tone mapping method to obtain excellent image quality, but over satuated can happen in the zones that have quickly changes with the depth of field. In Narasimhan's [20] work, he came up with a novel technology based on atmosphere scattering model and acquired the depth data by comparing two outdoor images in the same scene. While under different weather conditions, however, that approach can easily affected by halo effect problem.

In short, there are major problems in the above mentioned algorithms: (1) Due to the insufficient precision of the transmission, their haze removal algorithms result in over saturation and/or halo effect. (2) The heterogeneous atmospheric light should be fully considered. If not, underexposure and/or hue error issues can often be brought about. Inspired by the above mentioned analysis, based on the atmospheric scattering model, the author adopts a novel haze removal method to recover fog images. This method can be divided into two sections. First, to get an atmosphere light value by a combination of canny edge detection and binary-tree decomposition, which can obviously ameliorate the accuracy of parameters. Second, to handle the transmission by adopting adaptive wiener filter and morphological processing technique. Compared with the existing mainstream de-hazing algorithms, the improved algorithm can achieve better visual effect and color fidelity.

2. Background Theory

Compared with the techniques that merely consider the visual impact, utilizing a physical optics model will improve the accuracy of results. The attenuation and scattering of the radiance of atmospheric light in a propagation medium satisfies the radiative transfer equation (RTE) [21]. RTE is a well balanced equation describing the essence of the scattering process which includes both energy loss due to attenuation and scattering, and gain due to multiple forward scattering. Based on its three dimensional property, the realistic structure of clouds can be turned into a physical model. And the structure property of cloud can be used as an input to RTE.

In the three-dimensional coordinate system, according to the Beer's law [22], the received light intensity, in other words, transmission $t(s)$ can be expressed as an exponentially decaying function of depth of field $d(s)$, as shown in (1)

$$t(s) = e^{-\beta d(s)} \tag{1}$$

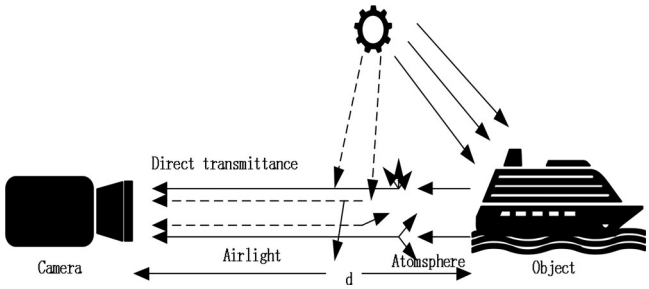

Fig. 1. Attenuation model.

RTE is the extension of Beer's law, through which the variation of energy is achieved by balancing the loss caused by attenuation and scattering. RTE is given by formula (2).

$$-\frac{dR(s,\Omega)}{\beta ds} = R(s,\Omega) - F(s,\Omega) \tag{2}$$

Here, β is defined as the dissipation coefficient, $R(s,\Omega)$ the scene radiance, s the distance between transmitter and $\Omega(\omega, \Phi)$, ω and Φ the inclination and azimuthal angles respectively.

In the field of two-dimensional image processing, the physics expression of the transmission $t(x, y)$ can be represented as (3):

$$t(x,y) = e^{-\beta d(x,y)} \tag{3}$$

Here, $d(x, y)$ represents depth of field, $t(x, y)$ transmission. In the field of computer images and visual application system, the physical optics model of atmospheric light [20], [23] has been broadly used to characterize the construction of fog images. On the basis of RET, it can be further divided into attenuated model and scattering model, which are demonstrated in Fig. 1, and formulated in (4):

$$F(x,y) = A\rho e^{-\beta d(x,y)} + A(1 - e^{-\beta d(x,y)}) \tag{4}$$

Where (x, y) indicates a pixel position, $F(x, y)$ the observed intensity of a fog image. ρ represents the normalized radiance, A the radiance of atmospheric light, which is generally acknowledged as the pixel value of an image with maximum intensity.

The objective of this paper is to obtain an approximate scene radiance of a fog-free image $R(x, y)$, which stands for the reflectivity of the scene point from the observer's angel. $R(x, y)$ can be calculated by multiplying the normalized radiance with the atmospheric light radiance, as shown in (5).

$$R(x,y) = A\rho \tag{5}$$

On the basis of (3) and (5), Formula (6) can be exported.

$$F(x,y) = R(x,y)t(x,y) + A(1 - t(x,y)) \tag{6}$$

From the perspective of computer graphics, the equation of the ambient light physical optics model indicates that the radiance of atmospheric light A holds a geometric correlation with $F(x, y)$ and $R(x, y)$, and the ratio of two line segments can be defined as transmission $t(x, y)$. The mathematical relation model Figure is shown in Fig. 2.

$$t(x,y) = \frac{\|A - F(x,y)\|}{\|A - \mathrm{R}(x,y)\|} = \frac{A^C - F(x,y)}{A^C - \mathrm{R}(x,y)} \quad C \in [R, G, B] \tag{7}$$

The dark channel prior (DCP) is built upon the constant observations of the outdoor fog-free images: in vast majority cases, there exists at least one color channel with extremely low intensity

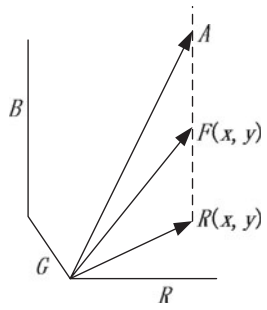

Fig. 2. Mathematical relation model of transmittance t(x, y).

value. Based on the definition of the DCP, we suppose that R(x, y) is the fog-free image without sky area, and its value of dark channel is quite low and approximates 0.

$$R^{\text{dark}}(x, y) \to 0 \tag{8}$$

We find there are mainly three factors that can cause the extremely low pixel value in dark channel: 1. shadows (such as the shadows of buildings in urban landscape and automobiles); 2. colorful objectives or surfaces of objects (such as the green plants, red, yellow or blue objects); 3. dark objectives. These factors combined can result in the low pixel value in dark channel.

Supposing that R, G, B color channel of the radiance of atmospheric light A^C has been given, then formula (6) can be transformed to (9) through A^C.

$$\frac{F^C(x, y)}{A^C} = t(x, y)\frac{R^C(x, y)}{A^C} + 1 - t(x, y) \tag{9}$$

Owing to the fact that every color channel is independent, we make calculation to both side of the dark channel equation by assuming that transmission will remain unchanged at $\Omega(x, y)$ and describing the transmission as $t(x, y)$.

$$\min_{Z\in\Omega(x,y)}\left(\min_{C\in[r,g,b]}\left(\frac{F^C(x, y)}{A^C}\right)\right) = t(x, y)\min_{Z\in\Omega(x,y)}\left(\min_{C\in[r,g,b]}\left(\frac{R^C(x, y)}{A^C}\right)\right) + 1 - t(x, y) \tag{10}$$

As R(x, y) is a fogfree image, the dark channel value of R(x, y) approximates 0 according to dark channel prior theory.

$$R^{\text{dark}}(x, y) = \min_{C\in[r,g,b]}(\min_{Z\in\Omega(x,y)}(R^C(Z))) = 0 \tag{11}$$

Here, A^C is a positive value, so (12) can be derived.

$$R^{\text{dark}}(x, y) = \min_{C\in[r,g,b]}\left(\min_{Z\in\Omega(x,y)}\left(\frac{R^C(x, y)}{A^C}\right)\right) = 0 \tag{12}$$

The deduced expression of the transmission t(x, y) can be calculated as follow. Combine (10) with (12), then one term can be eliminated and t(x, y) is given by:

$$t(x, y) = 1 - \min_{Z\in\Omega(x,y)}\left(\min_{C\in[r,g,b]}\left(\frac{F^C(x, y)}{A^C}\right)\right) \tag{13}$$

In order to make the haze removal results more natural and maintain a positive perception of depth [3], we retain small amount of fog for long-distance objectives, and introduce modulus w_0 into (14) for adjustment. The value of w_0 is averagely set as 0.95, so t(x, y) is expressed as:

$$t(x, y) = 1 - w_0\min_{Z\in\Omega(x,y)}\left(\min_{C\in[r,g,b]}\left(\frac{F^C(x, y)}{A^C}\right)\right) \quad 0 \le w_0 \le 1 \tag{14}$$

U and L are unit matrixes with the same size. Taking the value of λ as the correcting parameter, He [17] adopt soft matting algorithm to get the improved transmission t_1(x, y).

$$(L + \lambda U)t(x, y) = \lambda t_1(x, y) \tag{15}$$

3. The Radiance of Atmospheric Light A

In many de-hazing algorithms, strong visual effect areas in haze images are often selected for estimating the radiance of atmospheric light A, which leads to reflection matters. For example, surface of a reflective body is wrongly applied for the estimation of A. He [17], [18] chooses the top 1 percent of the maximal pixel value in the whole picture as the radiance of atmospheric light A, which leads to a low precision. In this paper, canny edge detection algorithm [24] is employed for edge detection to locate approximate area of the radiance of atmospheric light A. the maximal value of atmospheric light can be identified by binary-tree method. Hence, the radiance of atmospheric light A is obtained precisely. Besides, the efficiency of our algorithm can be improved by estimating transmission through adaptive wiener filter and image morphology.

3.1 Sky Area Location

In this paper, the edge in haze image $F(x, y)$ is detected by the canny edge detection algorithm [24]. In regard to fog images which contain the sky area, it could be discovered that the color of the scene is comparatively vivid, whereas the sky part are greyish white and homogeneous. So by using mean grey values of 8×8 pixel block to detect both sides of the edge, we can find smoothly connected region. Hence, the position of sky area s_1 can be roughly judged according to the characteristic of high pixel intensity of atmospheric light.

Canny edge detection algorithm [24] takes Gaussian function as smooth filter to process the haze image in the first place, that is, to remove noises in the image with Gaussian operator [25] by image convolution.

$$G(x, y) = \frac{1}{2\pi\sigma^2} \exp\left[\frac{-(x^2 + y^2)}{2\sigma^2}\right] \tag{16}$$

$$I(x, y) = (\nabla G(x, y)) * F(x, y) = \nabla(G(x, y) * F(x, y)) \tag{17}$$

In (16), σ is defined as the standard deviation. It's crucial to select the value of σbecause the precision of edge detection result depends on the selected value of σ. $G(x, y)$ is Gaussian function centered at pixel (x, y), ∇ is expressed as Gradient elution, $*$ represents the convolution operation, and the Gaussian process result $I(x, y)$ of haze image $F(x, y)$ can be derived in (17).

Edge point is defined as the local maximum intensity point in every gradient direction. Besides, discrete operator template is used for calculating the local gradient and the direction of every edge point. In this paper, finite difference of first-order partial is applied for calculating gradient direction and amplitude of the smoothed image $I(x, y)$. The partial derivative of x is given by (18), the partial derivative of y is given by (19).

$$P_x(x, y) = (I(x + 1, y) - I(x, y) + I(x + 1, y + 1) - I(x, y + 1))/2 \tag{18}$$

$$P_y(x, y) = (I(x, y + 1) - I(x, y) + I(x + 1, y + 1) - I(x + 1, y))/2 \tag{19}$$

Then, we use the norm and convert $P_x(x, y)$ and $P_y(x, y)$ to attain amplitude $M(x, y)$ and gradient direction $\theta(x, y)$. what's more, $M(x, y)$ represents edge strength of the pixel (x, y), $\theta(x, y)$ represents normal vector of the pixel (x, y).

$$M(x, y) = \sqrt{P_x(x, y)^2 + P_y(x, y)^2} \tag{20}$$

$$\theta(x, y) = \arctan(P_y(x, y)/P_x(x, y)) \tag{21}$$

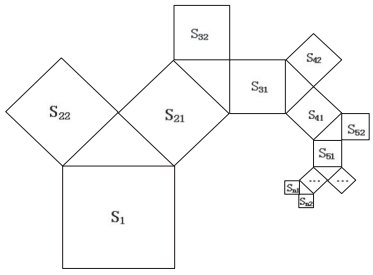

Fig. 3. Binary-tree decomposition model.

After the gradient direction is attained, we divide edges into 8 directions at the interval of 45 degrees.

Then we practice non-maximum suppression on gradient magnitude, and regard 2×2 neighbourhood of the pixel (x, y) as the major study object. The crucial point is comparing the intensity of $M(x, y)$ and adjacent pixels along the gradient direction. If intensity of $M(x, y)$ is bigger than the adjacent pixels, then the pixel (x, y) is perhaps the edge point, and it can be used for edge assessment. Or else, the pixel (x, y) is not the edge point and it should be marked as 0. Finally, we set two threshold values L_{th} and H_{th} after the non-maximum suppression. If $M(x, y) > H_{\text{th}}$, we could make sure that the pixel (x, y) is edge point. If $L_{\text{th}} < M(x, y) < H_{\text{th}}$, the pixel ($x$, y) should be judged whether it is the edge point or not. If $M(x, y) < L_{\text{th}}$, the pixel (x, y) is definitely not the edge point.

3.2 Estimation of the Radiance of Atmospheric Light A

To obtain the radiance of atmospheric light A precisely, the binary-tree decomposition model [26] is used for splitting the sky area s_1. The purpose of fundamental operation is to divide the area s_1 of the fog picture into two parts with equal area, set as area s_{21} and s_{22}. Then the mean grey values of the two parts are calculated. Comparisons are made between the bigger mean grey value set as $\bar{s}_{21}$, and the other one set as $\bar{s}_{22}$. Then we select area s_{21} for further division, get two sub-parts and repeat the same process. Absolute result d can be acquired by obtaining the difference of mean grey value $\bar{s}_{n1}$and 255. Repeat the above-mentioned steps until value d satisfies the criterion of smaller than the given threshold value t, and $\bar{s}_{n1}$ is the radiance of atmospheric light A, as show in (22) and (23). The process of binary-tree division is shown as Fig. 3, and the process of estimation of A is shown as Fig. 4.

$$d = |255 - \bar{s}_{n1}| \tag{22}$$

$$\begin{cases} \boldsymbol{A} = \bar{s}_{n1} & d < t \\ \boldsymbol{A} \neq \bar{s}_{n1} & d \geq t \end{cases} \tag{23}$$

4. Transmission

Owing to the different impact of atmospheric light, the effectiveness of image de-hazing changes with distance from view to watcher. Generally speaking, the luminance of images are incrementally increased as haze thickens. With the priori information of haze image and the radiance of atmospheric light A, t(x, y) can be roughly estimated, as show in (13). However, transmission changes with the depth of field and especially rapid in the area of edges, besides, there exists halo effect on edges of de-hazing images. So He [17] applied soft-matting algorithm with large lap matrix to process transmission. This processing is featured with great cost and long-time consumption; meanwhile, the calculation of t(x, y) takes up the most of process time. Therefore, He applied guide filter [18] to reduce the cost of computation. However, it still takes up a lot of processing time. Hence, this paper optimizes transmission with adaptive wiener filter as well as image morphology methods.

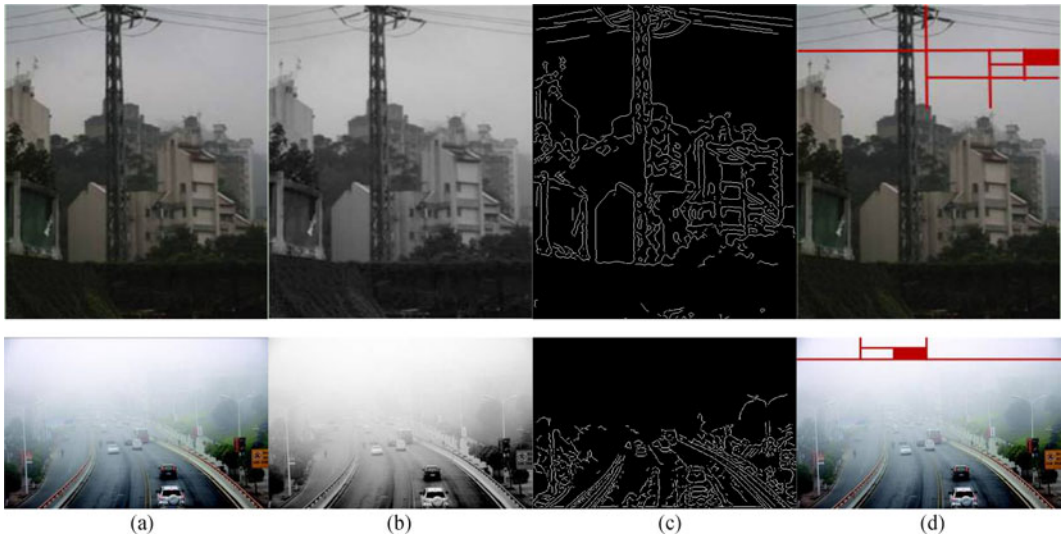

Fig. 4. Methods of obtain A based on canny edge detection and binary-tree algorithm. (a) Fog image. (b) Greyscale. (c) Canny edge detection. (d) Binary-tree algorithm.

4.1 Transmission Optimization

Wiener filter is broadly applied in image restoration. This technology has both impressive and compelling impact on the degraded images restoration and the capability of anti-noise. In addition, the time consumption of wiener filter is little owing to its low computation. Considering that the transmission t(x, y) and depth of field are in exponential relationship as expressed in (3), it is hardly to avoid large deviations on field of depth along the edges. Besides, there exists severe ring effect on edge areas in haze images. The selected filter algorithms should keep as many edge details as possible while removing noises. Wiener filter [27] has significant effect in removing noises and creating good visual sensory experience, whereas can easily affected by ring artifacts. In this paper, the adaptive wiener filter [27] is selected for processing transmission, which can avoid deficiencies of traditional wiener filter.

The convolution model of minimum mean square error is transformed to frequency domain expression in traditional wiener filter. As shown in (24).

$$T_1(u, v) = \frac{\mathrm{H}^*(u, v)}{|\mathrm{H}(u, v)|^2 + |S_n(u, v)/S_f(u, v)|} \bullet T(u, v) \tag{24}$$

In it, H(u, v) and T(u, v) are Fourier conversions of point spread function (PSF) h(x, y) and transmission image t(x, y); $H*$ (u, v) is complex conjugate of H(u, v); S_{f}(u, v) is power spectrum of the original image; S_{n}(u ,v) is noise power spectrum, and T_1(u, v) is the Fourier conversion of transmission image t(x, y).

$$\gamma = S_n(u, v)/S_f(u, v) \tag{25}$$

An image can be divided into three areas: flat area, vein area and edge area in the adaptive wiener filter [27]. When $\gamma_{\mathrm{flat}} = 10^{-2}$, $\gamma_{\mathrm{vein}} = 10^{-3}$ and $\gamma_{\mathrm{vein}} = 10^{-5}$, the recovered images which be given consideration to brightness, edge preservation and the degree of de-noising [28] are achieved to the optimum state. In traditional Wiener filter, however, the whole process set a unified parameter

$\gamma = 10^{-5}$.

$$m_{local}(x, y) = \frac{1}{(2P+1)(2Q+1)} \sum_{i=x-P}^{x+P} \sum_{j=y-Q}^{y+Q} t(i, j) \tag{26}$$

$$\delta_{local}(x, y) = \frac{1}{(2P+1)(2Q+1)} \sum_{i=x-P}^{x+P} \sum_{j=y-Q}^{y+Q} [t(i, j) - m_{local}(x, y)]^2 \tag{27}$$

Here, m_{local}(x, y) refers to local mean value; δ_{local}(x, y) is expressed as local variance; (x, y) indicates the pixel of the transmission map; $2P + 1$ and $2Q + 1$ refer to sizes of the used template. Due to the selected template should be matched with blocks of dark channel images, 15×15 template is selected. Then we calculate the mean value and variance of pixel values $(2P + 1) \times (2Q + 1)$ surrounding (x, y).

In this section, firstly, the improved approach calculate local variance of initial transmission map while attaining and storing maximal local variance δ_{maxlocal}(x, y), After that, we divide the image into three areas as mentioned above and compute the value ofγ, respectively. The adaptive wiener filter can basically eliminate the blocking effect in transmission map. However, there is deviation between edges of the processed transmission map and haze image F(x, y), so the further procedure is required.

4.2 Block Effect Reduction

In this paper, Fourier inversion is applied on $T_1(x, y)$ to attain $t_1(x, y)$; then the follow-up processing of $t_1(x, y)$ is practiced with image morphology approach by method of opening. In order to keep detail of de-hazing image and mutation area of depth of field, image erosion processing Θ is firstly applied to inwardly narrow down the edges;then practice dilation operation $\odot$ to connect some scattered details on the edges. Owing to the fact of the pixel value of transmission is binarized, indeed, the objective of image opening technology used here is to attain the maximum value in the de-blocking area.

$$t_2(x, y) = \odot(\Theta t_1(x, y)) \tag{28}$$

The extend of erosion [29] processing on $t_2(x, y)$ depends on the size of the block. Too high or too low degree of erosion [29] will result in unmatched edges with original image $F(x, y)$. In general, it is 1/2 of the block. Compared with He [18], the optimized transmission obtained more overall information and it's edge parts are close to natural state. As shown in the Fig. 5, the way of optimizing transmission by combining the adaptive wiener filter with image morphology [30] algorithm is feasible.

4.3 Image Scene Restoration

As the radiance of atmospheric light A and the transmission are obtained, in the basis of (6), the fogless image scene R(x, y) can be given by (29).

$$R^C(x, y) = \frac{F^C(x, y) - A^C}{\max\{t_2(x, y), t_0\}} + A^C \tag{29}$$

Here, t_o is a low limit of the transmission and set as 0.1 according to the empiric value. Fig. 6 show the procedure of our method.

5. Experimental Results Comparison and Analysis

In order to verify the performance of our algorithm, a large number of experiments have been conducted. Our method and the following approaches are verified by MATLAB 17a software environment with configuration of Pentium (R) D, E6700 GHz CPU and 8 GB memory on computer.

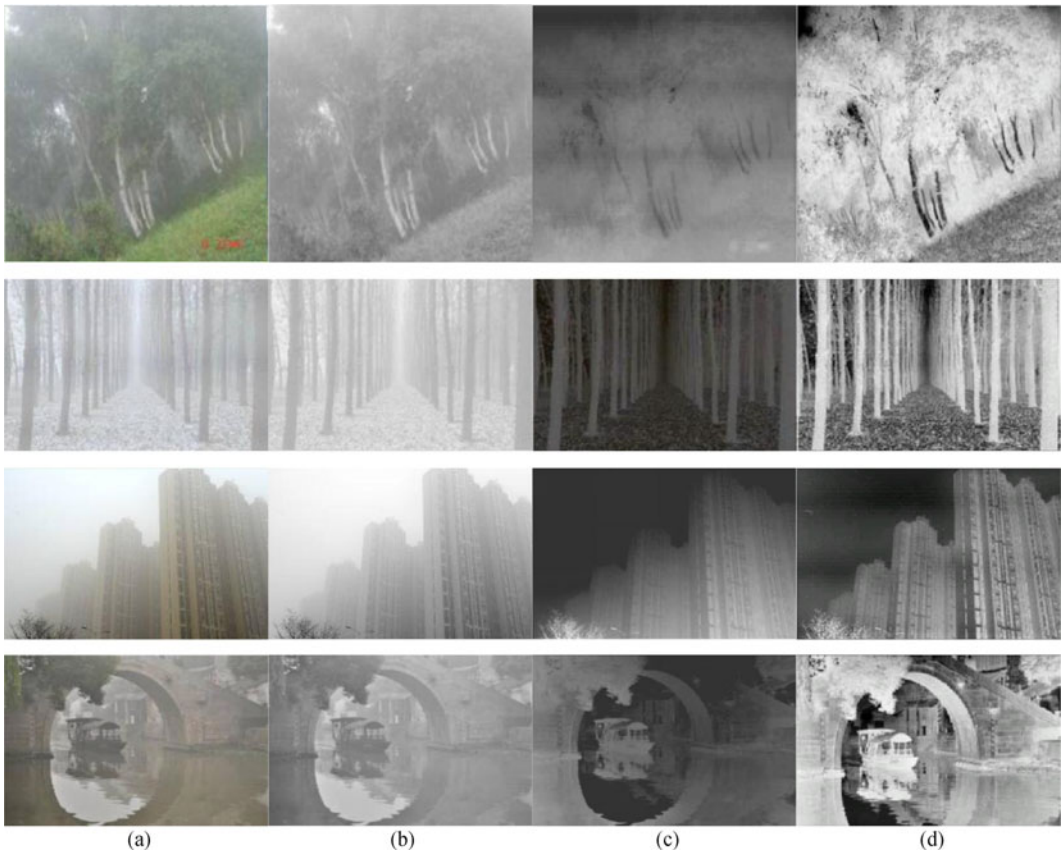

Fig. 5. The output of transmission processed by combining the improved partition Wiener filtering with image morphology. (a) Fog image. (b) Greyscale. (c) Original transmission. (d) Improved transmission.

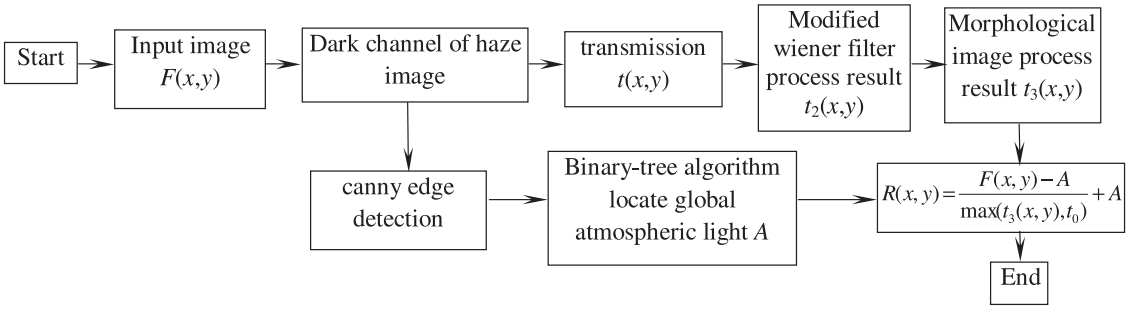

Fig. 6. Improved algorithm flowchart.

The algorithm [11], [18], [19] are restoration de-hazing algorithms based on physical optics model, and the algorithm [8] is an enhancement haze removal algorithm; the above well-known techniques all possess good de-hazing abilities. The experiment results are given and analyzed by comparing our approach with aforementioned algorithms.

We create our own image test suite, including 512 out-of-door fog images obtained by internet or taking pictures, containing multifarious of ordinary scenes. Natural landscape, buildings, trees, lake scenes, aerial-view photos, the distant view, and the near view are covered, which used in the experiments parts 5.2 as well as 5.3.

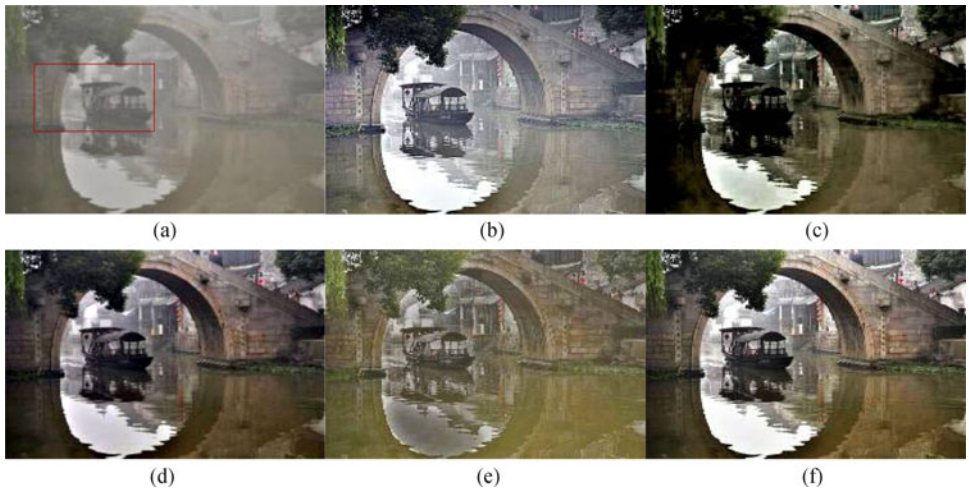

Fig. 7. Comparison of different de-hazing algorithms. (a) Fog image.(b) The algorithm [8]. (c) The algorithm [11]. (d) The algorithm [18]. (e) The algorithm [19]. (f) Improved algorithm.

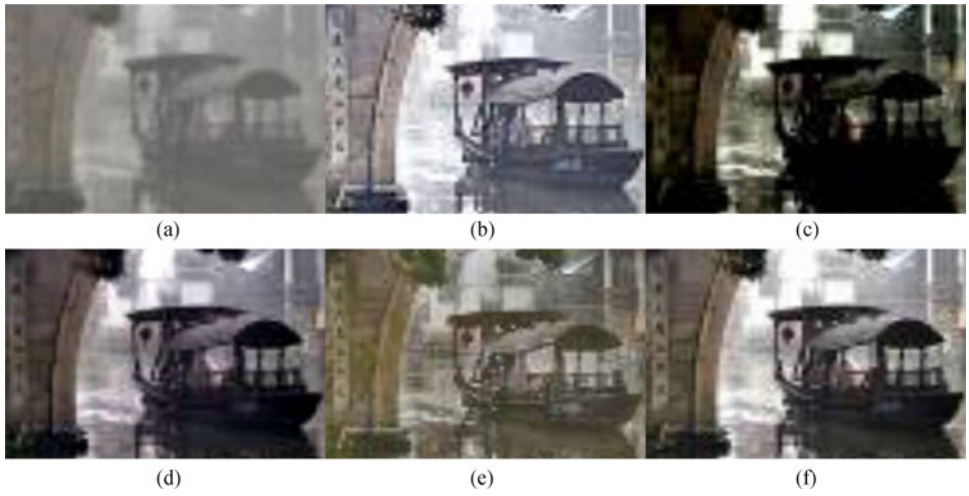

Fig. 8. Zoomed version results of different de-hazing algorithms. (a) Fog image.(b) The algorithm [8]. (c) The algorithm [11]. (d) The algorithm [18]. (e) The algorithm [19]. (f) Improved algorithm.

5.1 Subjective Vision

Without losing the integrity, we choose the different kinds of fog images from test suite and apply them in experiments. The following illustrations show the different image restoration results of de-hazing algorithms, and the scenes are pavilion (resolution ratio: 300 $*$ 500), buildings (resolution ratio: 400 $*$ 600), trees (resolution ratio: 600 $*$ 800). In Figs. 7, 9, 11, (a) is the original fog image, (b), (c), (d), (e), (f) are the de-hazing results. and In Figs. 8, 10, 12, there are zoomed version of above figures.

Fig. 7 shows the comparison of our approach and four advanced image haze removal techniques [8], [11], [18], [19]. In Fig. 7(a), a large portion of the lake occupies the entire picture, which can pose a challenge to de-hazing process and easily cause mirror reflection problem. In Fig. 7(b), the picture contrast is significantly strengthen, and the over enhancement problem of the method [8] leads to color shift. As we can see, the local area of the Fig. 7(c) has a significant distortion. The estimation of the radiance of atmospheric light A is inaccurate because of specular reflection problem, so the

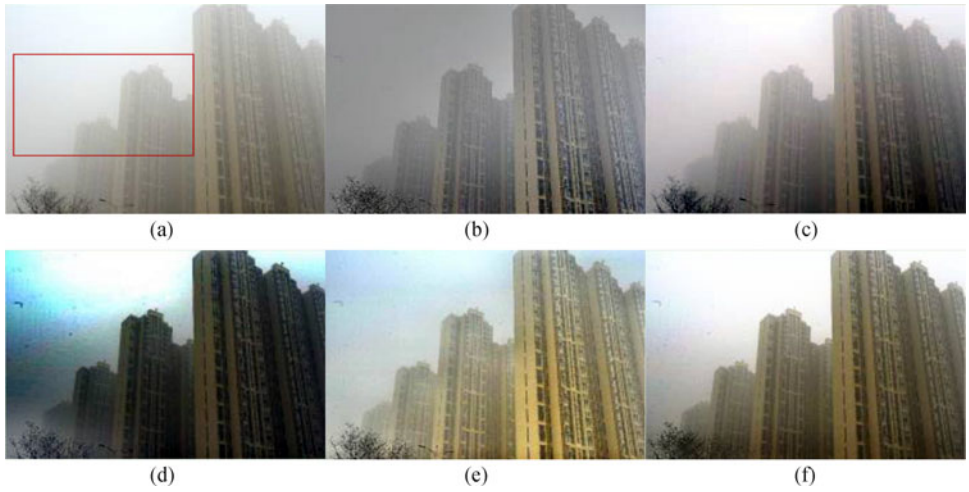

Fig. 9. Comparison of different de-hazing algorithms. (a) Fog image.(b) The algorithm [8]. (c) The algorithm [11]. (d) The algorithm [18]. (e) The algorithm [19]. (f) Improved algorithm.

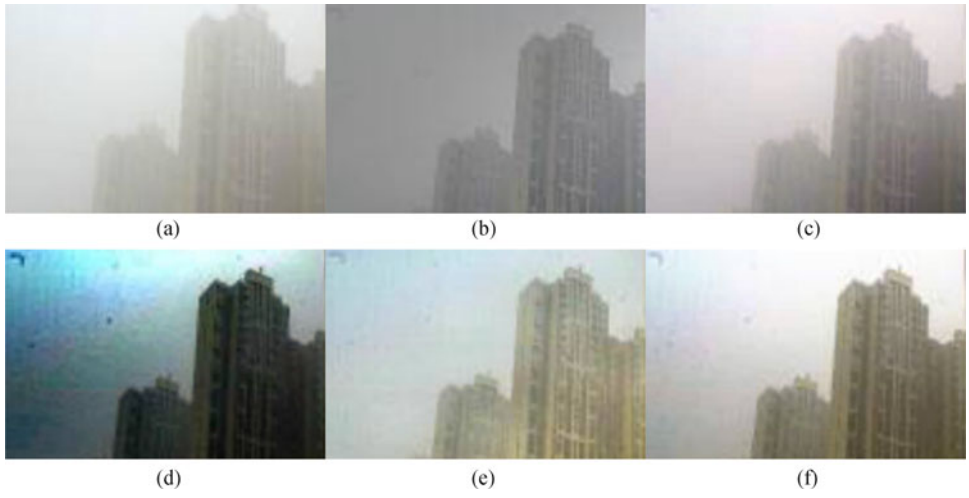

Fig. 10. Zoomed version results of different de-hazing algorithms. (a) Fog image.(b) The algorithm [8]. (c) The algorithm [11]. (d) The algorithm [18]. (e) The algorithm [19]. (f) Improved algorithm.

luminance of Fig. 7(d) is a little dark. The edge details of Fig. 7(e) are not clear enough, and halo effect is existed in the edge. We can verify it clearly in the zoomed version Fig. 8(e). While the Figs. 7(f) and 8(f) show the improved algorithm has bright image foreground color, in addition, a small part of the fog reserved which makes the image more real, and also emphasizes the details.

Fig. 9(a) presents a dense fog scene, however, directed at the sky regions in de-hazing images, both image noise and chromatic aberration are there when adopting the algorithm [11] and the algorithm [19], as we can see in Fig. 9(c) and (e). The above reason is the reality that the obtained transmission is imprecise, so amplifying the noise and color gamut in a large range. Though the sky region is salient after handled by the algorithm [18], the color shift phenomena appeared in the boundary between sky region and non sky region, and we can see the detail from Fig. 10. Fig. 9(f) expresses the haze removal results adopting by our algorithm. As we can see, the fog is eliminated clearly and can not cover a large number of objects

Fig. 11 shows the haze removal results applying four kinds of de-hazing algorithms on the in-homogeneous illumination fog image. Fig. 11(b) result are incline to create distorted sky color,

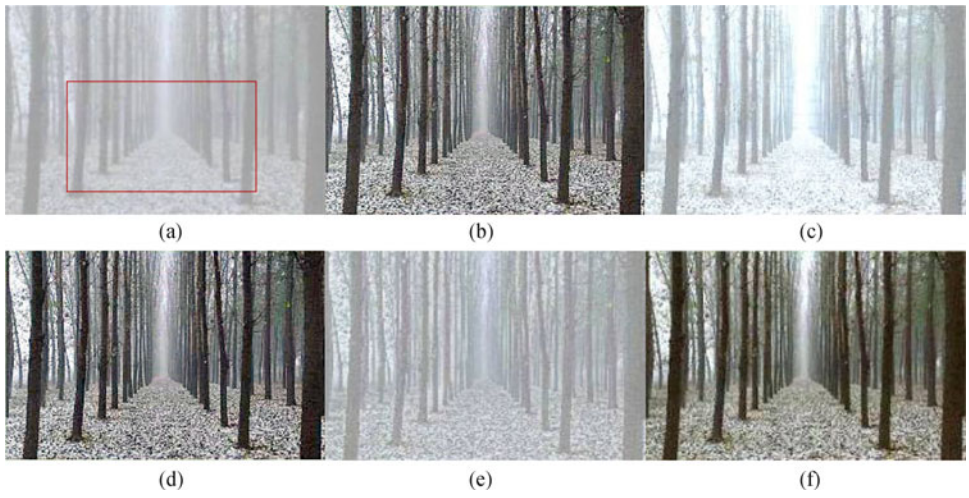

Fig. 11. Comparison of different de-hazing algorithms. (a) Fog image.(b) The algorithm [8]. (c) The algorithm [11]. (d) The algorithm [18]. (e) The algorithm [19]. (f) Improved algorithm.

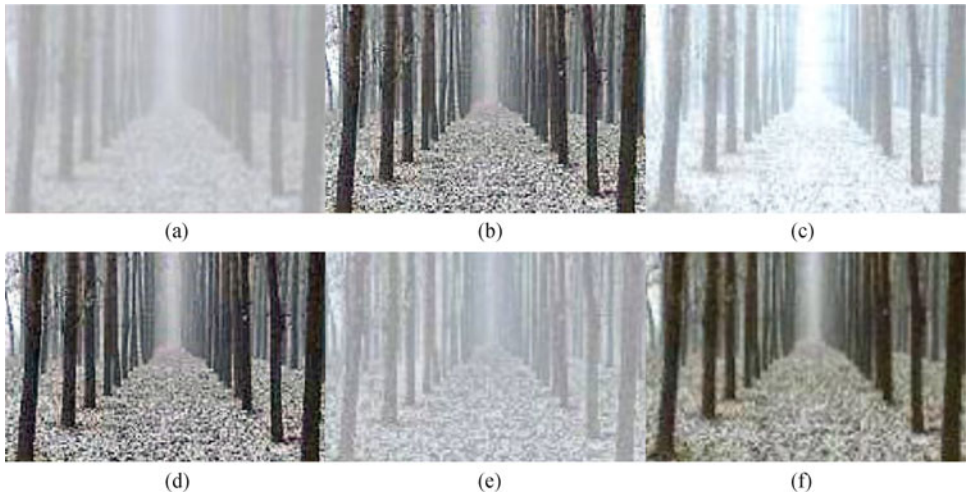

Fig. 12. Zoomed version results of different de-hazing algorithms. (a) Fog image. (b) The algorithm [8]. (c) The algorithm [11]. (d) The algorithm [18]. (e) The algorithm [19]. (f) Improved algorithm.

and the zoomed vision can show clearly. Fig. 11(c) contains plentiful details, whereas the visual impact is excessive enhanced. What's more, halo effect occurs nearby to the depth of mutations, owing to the poor transmission estimation behavior by surface albedo used in approach [11]. The method [18] can dramatically optimized the visual impact of the fog images, while the halo effect are happened in the area with dark subjects. In Fig. 11(e), we can see that the haze image recovered by the method [19] normally looks faint, and affected by gradient reversal effects. In comparison with the four methods, our approach behave better in terms of de-hazing capability.

5.2 Objective Evaluation

The behavior of our approach and four state-of-the-art de-hazing techniques are assessed by image information entropy (IIE) [31]. Besides, three notable quantitative indicators are introduced in [32],

TABLE 1
The Objective Evaluation of De-hazing Results

indicator	images	e	r	ϵ	IIE
Fog image	Fig.7(a)	0.5398	1.2539	0.3131	7.2979
	Fig.9(a)	0.7352	1.5887	0.1979	7.5732
	Fig.11(a)	1.0601	1.7569	0.1023	6.9031
The algorithm[8]	Fig.7(b)	0.9842	2.0022	0.1531	7.7012
	Fig.9(b)	1.2165	2.2359	0.1668	7.8816
	Fig.11(b)	1.4608	2.3571	1.2885	7.0941
The algorithm[11]	Fig.7(c)	1.1382	1.4889	0.1856	7.3989
	Fig.9(c)	0.6015	2.1578	0.3969	7.5515
	Fig.11(c)	1.2812	2.2869	0.1339	6.9918
The algorithm[18]	Fig.7(d)	0.6752	1.9132	0.0993	7.5163
	Fig.9(d)	0.9865	1.8654	0.2795	7.7152
	Fig.11(d)	1.5216	2.0131	0.0662	7.3285
The algorithm[19]	Fig.7(e)	0.4815	1.2792	0.3685	7.7035
	Fig.9(e)	0.5396	1.9746	0.1359	7.2979
	Fig.11(e)	1.1368	1.8531	0.0889	7.1079
The improved algorithm	Fig.7(f)	1.3965	2.1915	0.0678	7.9031
	Fig.9(f)	1.1754	2.3979	0.0896	7.6986
	Fig.11(f)	1.4862	2.3665	0.0521	7.4033

which consists of e, r and ϵ. Among the quantitative metrics above, IIE can be defined as follow:

$$IIE = -\sum_{w=0}^{I-1} \frac{F_w}{M \times N} \log \frac{F_w}{M \times N} \tag{30}$$

Here, M and N are defined as the pixel dimensions of length and width of an image individually. I means the highest gray level of the image, F_w represents the amount of pixels of the gray scale w, $F_w/(M \times N)$ is given by the chance of that the gray scale w showed in the image.

$$e = \frac{b_o - b_i}{b_i} \tag{31}$$

TABLE 2
Computing Expensive of Five Algorithms (Units:ms)

indicator	Resolution ratio	The algorithm[8]	The algorithm[11]	The algorithm[18]	The algorithm[19]	The improved algorithm
Fig.7	300*500	928	1517	8952	1341	1043
Fig.9	400*600	1128	2041	11375	1679	1205
Fig.11	600*800	1431	3179	13428	1926	1527

Where the index e expresses the ratio of newly visible edge recovered from the output of the de-hazing results. b_o and b_i represent the sum of visible edges in output and input images individually.

$$r = \exp[\frac{1}{b_o}\sum_{q_i \in \theta} \log(r_j)] \tag{32}$$

In it, r refers to the restoration quality of contrast in output images, and the computation procedure of which can be employed to estimate the average ratio of the gradients along the visible edges. q_i is relevant factor within the set Ψ, which contains visible edges of export images. r_j is defined as the ratio of the gradients among input and output images.

Whats more, index ϵ means the amount of pixels that may be excessively or inadequately exposed, and ϵ can be given by:

$$\varepsilon = \frac{n_t}{in_x \times in_y} \tag{33}$$

Here, n_t refines the total of pixels beyond the scope of possible, in_x and in_y represent the size of input images.

Generally speaking, the image information entropy reflects the degree of richness of image information. A higher result of IIE indicates that the haze removal result is more satisfactory and clear. Besides, e represents the complexity of image levels, in which a higher e means more levels and details. A high value of r indicates strong contrast and efficaciously enhanced edge details. While a smaller ϵ implies a better image quality.

From Table 1, in Fig. 9, the IIE metric of the haze removal by algorithm [18] is better than our approach. It is because that the algorithm [18] brings about over saturation and serious color cast in sky region, so that too much unwanted information can't be avoided in the haze removal results. In the IIE quality assessment, it can be perceived from Table 1 that in comparison with the other four advanced de-hazing algorithms, our approach has acquired a better result, which reveals the effectiveness of our method in both keeping clear image details and making high contrast.

The relevant assessment consequence of e, r and ϵ are also showed in Table 1. In short, our approach gains the highest value of e and r, and the smallest value of ϵ.

5.3 Time Complexity

In order to test the superiority of our method with regard to running time, various images with different sizes are adopted for observation. Comparing our approach with algorithm [8], [11], [18], [19], we find that the algorithm [18] in Table 2 has the poorest process efficiency because of the application of guide filter algorithm to handle sparse matrices, which leads to the drawback of expensive computing. The algorithm [11] is improved by adopting median filtering method, whereas it increases the execution time when the image resolution is increased. Algorithm [19] employs ICA algorithm, so the execution maintain fast along with the increase of image dimension, which

is even better than our approach. Algorithm [8] also has good performance because it adopts the Fast Fourier transform in the frequency domain for convolution operation.

6. Discussion and Conclusion

In the broadly used ambient light physical optics model, the accuracy of the radiance of atmospheric light and transmission valuation is the key point for haze removal effectiveness.

This paper innovates the estimation of unknown parameters of ambient light physical optics model, which includes the radiance of atmospheric light A and transmission $t(x, y)$. We determine the general range of the sky with canny edge detection algorithm on account of atmospheric light A, then use binary-tree decomposition model to conduct a search to this area, and replaces the soft matting of classical haze recovery method [18] with adaptive wiener filter on transmission.

There are some reasons for us to list here why we pick canny edge detector, adaptive wiener filter and binary-tree to improve the workflow. Canny operator takes Gaussian function as smooth filter to process the haze image. With Gaussian filter, the noises presented in an image can be removed, so this process will dramatically reduce the noises in haze removal results. Besides, With good localization and response properties, canny operator can produce accurate edge detection with thin and smooth edge.

The adaptive wiener filter has significant effect in creating good visual sensory experience. What's more, with adaptive wiener filter, the brightness and edge preservation in recovered images can be fully considered, and the degree of de-noising can be achieved to the optimum state. As for binary-tree, the primary advantages lie in its simplicity and high efficiency.

Compared with method [8], [11], [18], [19], though there are very little image noise and color shift in restored images by our method, the experimental results prove that the de-hazing images processed by our approach is clearer, more natural and efficient. And the color information recovery phenomenon, gradient reversal artifacts and halo effect can obviously be alleviated in our dehazing results.

Besides, our approach is especially effective for handling haze images with large proportion of sky regions. In future work, we plan to apply our still image haze removal approach to dynamic video processing. And with the purpose of improving processing efficiency, we plan to optimize canny edge detection algorithm and adaptive wiener filter.

Acknowledgment

The authors would like to thank the anonymous reviewers for their valuable suggestions.

References

[1] S. G. Narasimhan and S. K. Nayar, "Chromatic framework for vision in bad weather," in *Proc IEEE Conf. Comput. Vis. Pattern Recognit*, Washington, DC, USA, 2000, pp. 598–605.
[2] C. Xiao and J. Gan, "Fast image dehazing using guided joint bilateral filter," *Vis. Comput.*, vol. 6, no. 28, pp. 713–721, 2012.
[3] J. Wang, N. He, L. Zhang, and K. Lu, "Single image dehazing with a physical model and dark channel prior," *Neurocomputing*, vol. 149, pp. 718–728, 2013.
[4] B. H. Chen, S. C. Huang, and J. H. Ye, "Hazy image restoration by Bi-histogram modification," *ACM Trans. Intell. Syst.*, vol. 4, no. 6, pp. 50-1–50-17, 2015.
[5] C. H. Xie, Y. Q. Song, and J. M. Chen, "Fast medical image mixture density clustering segmentation using stratification sampling and kernel density estimation," *Signal Image Video Process*, vol. 2, no. 5, pp. 257–267, 2011.
[6] L. Zhong, Y. Shang, and X. Zhou, "Fast single image dehazing based on a regression model," *Neurocomputing*, vol. 245, pp. 180–191, 2017.
[7] A. Rizzi, C. Gatta, and D. Marini, "From Retinex to automatic color equalization issues in developing a new algorithm for unsupervised color equation," *J. Electron. Imag.*, vol. 1, no. 13, pp. 75–84, 2004.
[8] G. D. Finlayson, M. S. Drew, and C. Lu, "Entropy minimization for shadow removal," *Int. J. Comput. Vision*, vol. 1, no. 85, pp. 35–37, 2009.
[9] E. Flato, F. Fogel, H. Dan, and E. Leiserowitz, "Exact minkowski sums and applications," in *Proc. 18th ACM Symp. Comput. Geometry*, 2002, pp. 273–274.
[10] R. Fattal, "Single image dehazing," *ACM Trans. Graph.*, vol. 3, no. 27, pp. 1–9, 2008.

[11] D. Singh and V. Kumar, "Dehazing of remote sensing images using improved restoration model based darkchannel prior," *Imag. Sci. J.*, vol. 65, no. 5, pp. 182–192, 2017.
[12] R. Tan, "Visibility in bad weather from a single image," in *Proc IEEE Conf. Comput. Vis. Pattern Recognit.*, Washington, DC, USA, 2008, pp. 1–8.
[13] K. He, J. Sun, and X. O. Tang, "Single image haze removal using dark channel prior," in *Proc IEEE Conf. Comput. Vis. Pattern Recognit.*, Washington, DC, USA, 2009, pp. 1956–1963.
[14] Z. Luan, Y. Shang, X. Zhou, Z. Shao, and G. Guo, "Fast single image dehazing based on a regression model," *Neurocomputing*, vol. 245, pp. 10–22, 2017.
[15] C. H. Xie, W. W. Qiao, Z. Liu, and W. H. Ying, "Single image dehazing using kernel regression model and dark channel prior," in *Signal, Image Video Process.*, vol. 11, no. 4, pp. 705–712, 2017.
[16] J. G. Jiang, T. F. Hou, and M. B. Qi, "Improved image dehazing algorithm based on dark channel prior," *J. Circ. Syst.*, vol. 2, no. 16, pp. 7–12, 2011.
[17] K. He, J. Sun, and X. Tang, "Single image haze removal using dark channel prior," *IEEE Trans. Pattern Anal.*, vol. 12, no. 33, pp. 2341–2353, Dec. 2011.
[18] K. He, J. Sun, and X. Tang, "Guided image filtering," *IEEE Trans. Pattern Anal. Mach. Intell*, vol. 6, no. 35, pp. 1397–1409, Jun. 2013.
[19] J. P. Tarel and N. Hautiere, "Fast visibility restoration from a single color or gray level image," in *Proc. IEEE Int. Conf. Comput. Vis.*, 2009, pp. 2201–2208.
[20] S. G. Narasimhan and S. K. Nayar, "Contrast restoration of weather degraded images," *IEEE Trans. Pattern Anal. Mach. Intell.*, vol. 25, no. 6, pp. 713–724, Jun. 2003.
[21] K. N. Liou and N. Rao, "Radiative transfer in cirrus clouds part IV: On cloud geometry inhomogeneity and absorption," *J. Atmospheric Sci.*, vol. 53, no. 21, pp. 3046–3065, 1996.
[22] J. M. Parnis and K. B. Oldham, "Beyond the Beer–Lambert law: The dependence of absorbance on time in photochemistry," *J. Photochem. Photobiol. A Chem.*, vol. 267, no. 9, pp. 6–10, 2013.
[23] S. G. Narasimhan and S. K. Nayar, "Vision and the atmosphere," *Int. J. Comput. Vis.*, vol. 3, no. 48, pp. 233–254, 2002.
[24] K. Khongkraphan, "An efficient color edge detection using the mahalanobis distance," *J. Inf. Process. Syst.*, vol. 10, no. 4, pp. 589–601, 2014.
[25] J. L. Gracia and E. O'Riordan, "A singularly perturbed convection–diffusion problem with a moving pulse," *J. Comput. Appl. Math.*, vol. 321, pp. 371–388, 2017.
[26] H. Pan, X. B. Li, and L. Z. Jin, "Object description and recognition using multiscale geometric analysis," *J. Infrared Millimeter Waves*, vol. 30, no. 1, pp. 85–90, 2011.
[27] D. K. Ramanah, G. Lavaux, and B. D. Wandelt, "Wiener filter reloaded: Fast signal reconstruction without preconditioning," *Monthly Notices Roy. Astronomical Soc.*, vol. 2, no. 468, pp. 1782–1793, 2017.
[28] F. Angelini, V. Bruni, I. Selesnick, and D. Vitulano, "Adaptive scale selection for multiscale image denoising," in *Advanced Concepts for Intelligent Vision Systems*, New York, NY, USA: Springer, 2015.
[29] R. C. Gonzalez and R. E. Woods, *Digital Image Processing*, 2nd ed. Beijing, China: Publishing House Electron. Ind., 2007, pp. 325–329.
[30] L. U. Vinzons, L. Shu, S. P. Yip, C. Y. Wong, and L. L. H. Chan, "Unraveling the morphological evolution and etching kinetics of porous silicon nanowires during metal-assisted chemical etching," *Nanoscale Res. Lett.*, vol. 12, no. 385, pp. 1–12, 2017.
[31] L. R. Nemzer, "Shannon information entropy in the canonical genetic code," *J. Theor. Biol.*, vol. 415, no. 21, pp. 158–170, 2017,
[32] N. Hautière, J. P. Tarel, D. Aubert, and E. Dumont, "Blind contrast enhancement assessment by gradient ratioing at visible edges," *Image Anal. Stereol.*, vol. 27, no. 2, pp. 87–95, 2008.